Int. J. Electrochem. Sci., 15 **(2020)** 9081 – 9087, doi: 10.20964/2020.09.36

International Journal of
ELECTROCHEMICAL
SCIENCE
www.electrochemsci.org

Enhanced Electrochemical Performances of Porous MnO as Anode material for Lithium Ion Batteries Prepared by Magnetic Field Assisted Hydrothermal Method

Yiyong Wei[1, 2,3], Shunjin Zhu[2], Jin Bai[2], Xiaohang Ma[1], Bangchuan Zhao[2], Xuebin Zhu[2], Zhenfa Zi[1,], Jianming Dai[2,*]*

[1] Department of New Energy, School of Physics and Materials Engineering, Hefei Normal University, Hefei 230601, China
[2] Key Laboratory of Materials Physics, Institute of Solid State Physics, Chinese Academy of Sciences, Hefei 230031, China
[3] University of Science and Technology of China, Hefei 230026, China
[*]E–mail: zfzi@issp.ac.cn (Z. Zi), jmdai@issp.ac.cn (J. Dai).

Received: 5 May 2020 / *Accepted:* 16 June 2020 / *Published:* 10 August 2020

Porous MnO prismoid was prepared by the magnetic-field assisted hydrothermal method. Influences of magnetic field (H = 2T) on microstructure, morphology, and electrochemical properties were studied. Under the action of magnetic field, X-ray diffraction results indicate that the crystal structure of MnO microprism is in accord with that of MnO microcube. SEM and TEM images suggest that the average grain size of MnO microprism decreases slightly. The electrochemical measurements show that MnO prismoid represents better than MnO microcube as the anode material for Lithium-ion batteries, which can be explained by the fact of modified crystal structure under the assistance of magnetic field.

Keywords: MnO prismoid; magnetic field; anode; lithium-ion batteries

1. INTRODUCTION

With the rapid consumption of energy, the demand for advanced lithium-ion batteries (LIB$_S$) is increasing [1]. Nevertheless, the current conventional anode materials is facing with some new challenges. It is necessary developing alternative anodes electrodes with super lithium storage capacity [2]. Transition metal oxides have attracted much attention due to their high theoretical specific capacity [3]. Especially, MnO displays momentous potential as anode in LIBs because of its high theoretical capacity (756 mAhg^{-1}) as well as low operating voltage, low-cost, earth abundance and nontoxic [4-5].

However, the large volume transformations during charge/discharge will lead to severe agglomeration and pulverization of MnO particles, which will result in the serious degradation in capacity and cycle lifetime [6-7]. To assuage these problems, porous nano-micro structure is a viable approach as previously reported, which displays evident improvement in property [8].

Some methods including hydrothermal, sol-gel and chemical solution deposition have been used to synthesize nanoscaled electrode material [9-11]. The hydrothermal method presents some advantages of high-product purity, good dispersibility, and easy control of particle size [12]. In this paper, a magnetic-field assisted hydrothermal method was used to synthesize porous MnO prismoid. The influence of magnetic field on structure, morphology and electrochemical properties were studied. Contrast with the MnO microcubes synthesized with zero magnetic field, the grain size of porous MnO prismoid became slightly larger, and the electrochemical performances were improved obviously.

2. EXPERIMENTAL

Porous MnO prismoid was synthesized utilizing $MnCl_2 \cdot 4H_2O$ and $(CO(NH_2)_2$ through facile magnetic-field-induced hydrothermal mehod. In preparation, 3 mmol $(CO(NH_2)_2$ and 2 mmol $MnCl_2 \cdot 4H_2O$ were dissolved in 20 mL deionized water and stirred vigorously for 40 minutes to obtain a clear solution. Afterwards the solution was shifted into a 30 mL Teflonlined stainless-steel autoclave and then sealed. The autoclave was kept at 200 °C for 15 h. The brown products were washed six times repeatedly with deionized water by centrifuging at 8000 rpm. The collected precursor was dried at 70 °C for 20 hours. For comparison the collected sample using 2T magnetic field was prepared under the same hydrothermal conditions as mentioned above. Lastly, the samples calcined at 500 °C for 6 hours under N_2/H_2 (5 vol% H_2) with a ramping rate of 2 °C per minute are marked as S0T and S2T, respectively.

The X-ray diffraction (XRD, D8 Discover, BRUKER AXS) was used to check microstructure and phase purity of the samples with Cu Kα radiation in 2θ range of 20°-80°. The field emission scanning electron microscopy (FESEM, SU8020, HITACHI) and the transmission electron microscopy (TEM, JEM-2010 JEOL) were used to study the morphology. The S2T electrodes were synthesized by coating slurry composed of active material (60 wt%), super P (30 wt%), and sodium carboxymethyl celluiose (CMC) binder (10 wt%) dispersed in a certain amount of deionized water on a Cu foil. It then dried at 80 °C for 18 hours in vacuum chamber, after that roll calendered. The mass loading of S2T is about 1.25 $mgcm^{-2}$. The coin cells were assembled in an argon filled glove box (MBraun Labmaster 130), where the contents of water and oxygen are less than 0.1 ppm applying produced electrode, a porous membrane separator (Celgard 3501) and an opposite electrode of lithium foil. The electrolyte was made up of 1.0 M $LiPF_6$ solution in dimethyl carbonate and ethylene carbonate (v/v, 1:1). Cyclic voltammetry (CV) curves were measured on an electrochemical workstation (CHI660E). Galvanostatic discharge/charge cycles were carried out between 0.01–3.0 V on a multi-channel LAMD battery cycling test system.

3. RESULTS AND DISCUSSION

Figure 1 displays XRD patterns of the S0T and S2T samples. For contrast, the standard XRD pattern of the MnO is also shown at the bottom of the figure1. The S2T shows similar XRD pattern with that of the S0T. The obvious diffraction peaks are in consistent with those indexed through JCPDS No. 075-0625, suggesting the synthesis of cubic-phase MnO with the group space of Fm-3m. However, the diffraction peak of S2T shifts to a lower angle than that of S0T in the corresponding enlarged XRD illustration, the result indicates that the mean crystallite size of S2T increases slightly due to applied magnetic field induction.

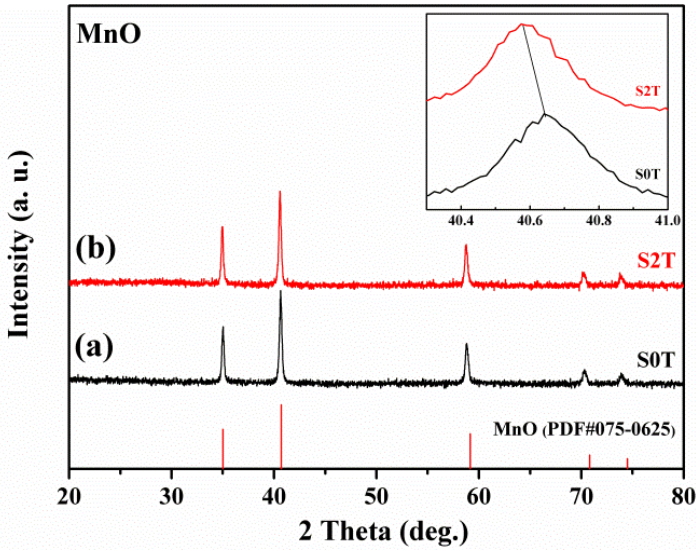

Figure 1. XRD patterns of the samples: (a) S0T; (b) S2T. Insets show the corresponding enlarged XRD patterns.

Figure 2a displays the SEM images of the hollow S0T microcubes with an average size above 8 um. The mesoporous S0T hollow microcubes were composed of a large number of nanoparticles with the mean size of around 61 nm (inset in figure 2a). The SEM image of S2T prismoid is shown in figure 2b. The prismoid is assembled of lots of microcubes kept nearly unchanged length by magnetic-field induced. The mesoporous prismoid can be proven by SEM images (inset in figure 2b). The TEM image could further confirm microstructure of S2T as revealed in figure 2c. The mesoporous hollow prismoid is composed of lots of S2T nanoparticles with the average size of around 56 nm (inset in figure 2c), which is almost in accordance with the SEM result. As exhibited in figure 2d, lattice plane spacing of S2T calculated from the HRTEM images is 0.26 nm along (111). The diffraction lines composed of diffraction spots in the selected area electron diffraction (SAED) model are shown inset in figure 2d, which could be ascribed to reflections of S2T, indicating low crystallization of the S2T.

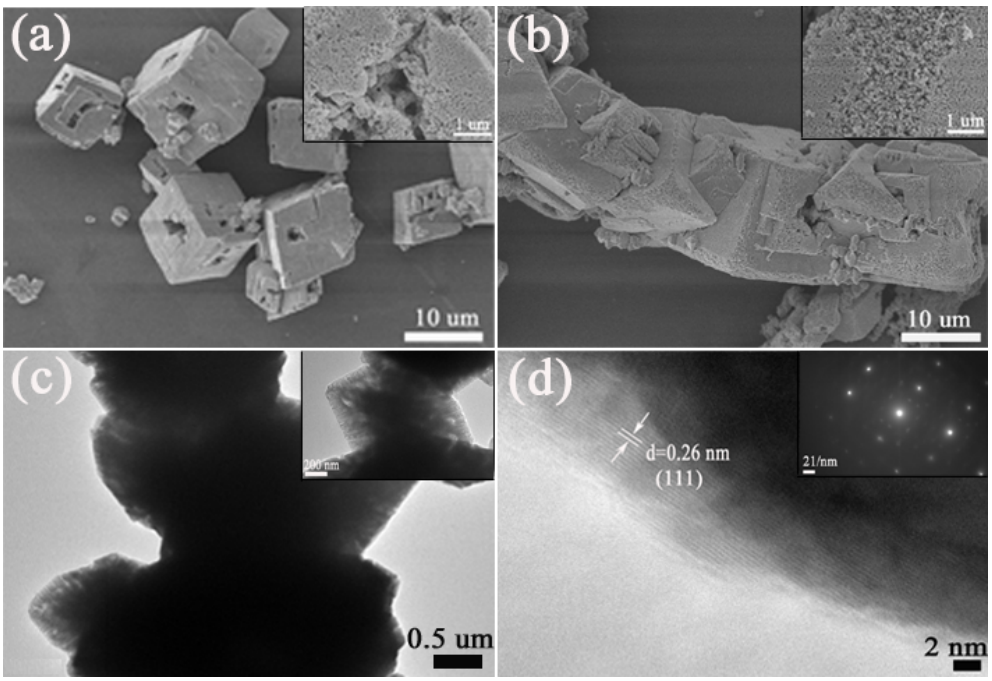

Figure 2. SEM images of S0T (a) and S2T (b), TEM (c) and HRTEM (d) images of S2T. Insets show the corresponding enlarged SEM and TEM pictures and SEAD pattern, respectively.

Table 1. Comparison of the electrode performance of MnO prismoid with the reported results.

MnO morphology	Current density (mA g^{-1})	Cycle number (Times)	Specific Capacity (mAh g^{-1})	Ref.
3D porous thin-flim	80	50	850.0	[31]
Nanocrystalline thin-flim	94.5	25	424.8	[24]
Porous nanoflake	246	200	708.4	[19]
mesoporous olive shape	98.3	200	782.8	[37]
hollow nanosphere	500	150	1050	[22]
Porous microsphere	50	50	704.0	[36]
Porous solid microcube	1000	495	425.5	[9]
Hexagonal Sheets	1000	500	821.5	[8]
Porous hollow microcube	378	200	923.0	[12]
Porous MnO prismoid	756	200	1044.6	This work

The electrochemical performances of the S0T and S2T as anode material for MnO/Li half cells have been researched. The capacity versus voltage (C-V) measurements of the S0T and S2T were performed in the voltage range of 0.01-3.0 V. The first discharge and charge capacities of the S0T electrode were 984.6 and 1257.0 $mAhg^{-1}$, respectively. However, the shape of the C-V profile changed evidently during subsequent cycles (figure 3a), indicating lower reversibility and structural stability during lithiation and delithiation. As for the S2T electrode, the initial discharge and charge capacities are 944.3 and 1240.2 $mAhg^{-1}$, respectively (figure 3b). Interestingly, the shapes of the charge/discharge curves are similar to each other from the first cycle, which suggests highly reversible lithium storage. The first three CV curves of S0T and S2T are shown in figure 3c-3d, which are consistent with the results of the first three charge/discharge tests. Moreover, In order to study the high-rate cycling property, the

S0T and S2T anodes were subjected to 200 long cycles at 1C (figure 3e). The initial discharge capacity of S2T is 1240.2 $mAhg^{-1}$, and the high discharge capacity of 1044.6 $mAhg^{-1}$ is maintained after 200 cycles, which is much higher than that of S0T with a discharge capacity of 969.9 $mAhg^{-1}$ after 200 cycles. As shown in Table 1, the mesoporous MnO prismoid is compared with the results reported in the literature, and its discharge specific capacity is better than that reported in the literature. Furthermore, S2T shows better rate property (figure 3f), exhibiting a 609.5 $mAhg^{-1}$ reversible discharge capacity at a current density of 1 C. Even if cycled at 4C and 8C cycles, the specific capacities reach 477.1 and 350.4 $mAhg^{-1}$, respectively.

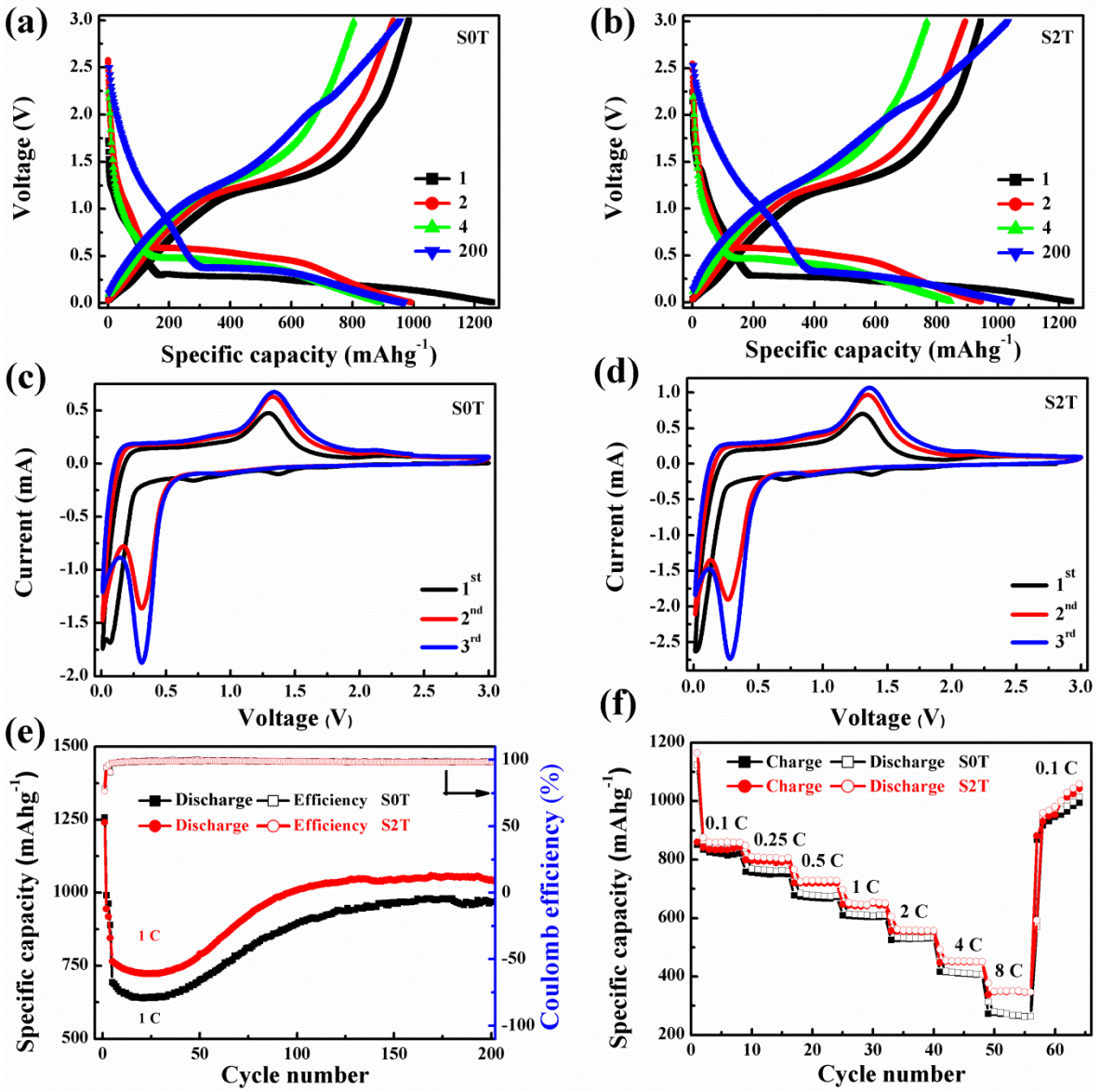

Figure 3. (a-b) Discharge-charge profiles, (c-d) CV curves, (e) cycling performances and (f) rate performances of S0T and S2T electrodes for LIBs.

In order to study the reason for the difference in electrochemical properties, electrochemical impedance spectroscopy (EIS) was measured. Nyquist plots of S0T and S2T after 200 cycles are shown in figure 4a. Both the curves exhibit arcs from high to low frequency range and a straight line inclined at approximately 45° in the low frequency range. Generally, the high-frequency semicircle can be attributed to the resistance of electrolyte (Rs), the SEI layer resistance (R_{SEI}), and the charge transfer resistance (Rct). The low frequency straight line is associated with Warburg impedance (σ) [13], indicating the resistance caused by ion diffusion. Remarkably, both the R_{SEI} and Rct values of S2T are smaller than those of S0T, The smallest R_{SEI} value of S2T suggests the pore prismoid hollow structure can protect S2T from side reactions with the electrolyte, forming a thinnest SEI film, while the lowest Rct value of S2T indicates a fastest electron transportation inside the S2T. Besides, the lithium diffusion coefficients of the two samples can be calculated from the low frequencies plots of EIS spectra (figure 4b) based on the following formulae [14, 15]:

$$Z' = R_s + R_{SEI} + R_{ct} + \sigma\omega^{-1/2} \quad (1)$$

$$D_{Li+} = (R^2T^2)/(2A^2n^4F^4C^2\sigma^2) \quad (2)$$

where ω, A, n, F, C, R, and T stand for the angular frequencies, electrode area, electrons number, Faraday constant and the molar concentration of Li ions, respectively. σ is the Warburg factor, which is related to Z' as shown in the above formula one and can be obtained from the slope of the lines of figure 4b. After linear fitting, the calculated Li^+ ion diffusion coefficients D_{Li}^+ of S0T and S2T are 1.762×10^{-14} and 4.167×10^{-14} cm^2 s^{-1} at 298 K, respectively. The enhanced ionic conductivity in S2T originates from two reasons, one stems from the shortened distance of ions diffusion due to the small size of nanoparticles, the other derives from the larger crystallite size of porous MnO prismoid in magnetic-field assisted hydrothermal process.

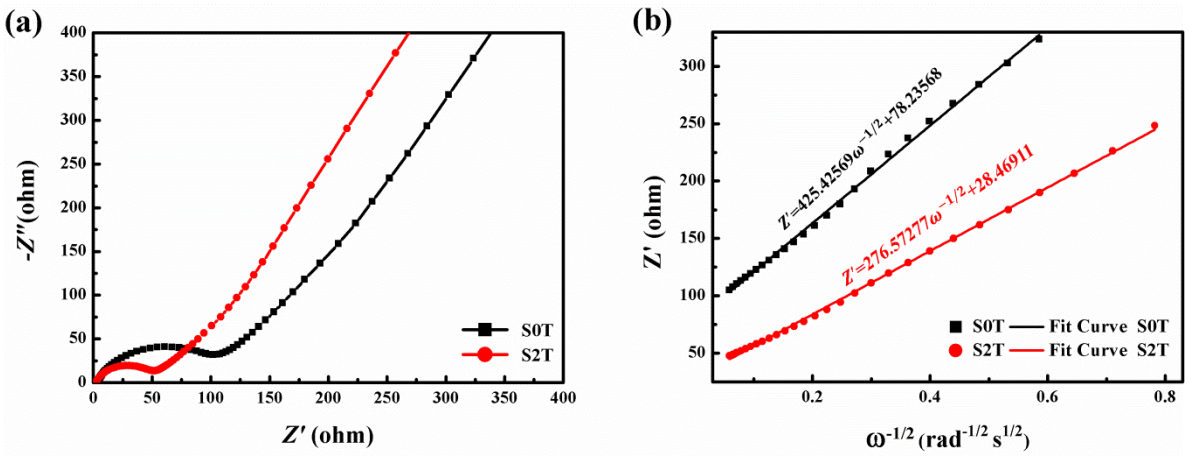

Figure 4. (a) Nyquist plot, (b) The relationship between Z' and $\omega^{-1/2}$ for S0T and S2T electrodes.

The excellent electrochemical properties of mesoporous S2T prismoid for LIBs can be mainly attributed to two aspects: Firstly, the nanostructured S2T shortens the diffusion path of lithium ions, being beneficial to the rate capability. Secondly, the abundant mesoporous S2T prismoid can make the electrolyte contact area large and accelerate the lithium-ion extraction/insertion reaction. Meanwhile the

substantial mesoporous hollow structure can provide effective void space to adapt to the volume change during the cycles, which can ameliorate the long cycling properties.

4. CONCLUSIONS

In summary, we studied magnetic-field-induced effects on porous S2T prismoid. The results indicate that the crystallite size of porous S2T prism increases slightly and the grain size decreases slightly after magnetic-field-induced hydrothermal treatment followed by calcining. The improved electrochemical performance can be reasonably explained by the induced action of magnetic-field.

ACKNOWLEDGEMENTS
This work is financially supported by the Visiting Project of Outstanding Talents in Anhui Provincial universities (Nos. gxgnfx2019024 and gxfxZD2016188), Anhui University Joint Key Laboratory Open Project Fund Project (No. 2019GDTC04), the National Nature Science Foundation of China (No. U1632161), and the Nature Science Research Project of Anhui province (Nos. 1808085QE154 and 1808085JQ13).

References

1. T. Yuan, Z. Tan, C. Ma, J. Yang, Z.F. Ma, S. Zheng*, Adv. Energy Mater.*, 7 (2017) 1601625.
2. C. Zhang, Y. He, P. Mu, X. Wang, Q. He, Y. Chen, J. Zeng, F. Wang, Y. Xu, J. X. Jiang, *Adv. Funct. Mater.*, 28 (2018) 1705432.
3. B. Kang, G. Ceder, *Nature*, 458 (2009) 190.
4. V. Aravindan, Y.S. Lee, S. Madhavi, *Adv. Energy Mater.*, 5 (2015) 1402225.
5. Y. Zhao, L.P. Wang, M.T. Sougrati, Z. Feng, Y. Leconte, A. Fisher, M. Srinivasan, Z. Xu, *Adv. Energy Mater.*, 7 (2017) 1601424.
6. J. Reed, G. Ceder, *Chem. Rev. ,* 104 (2004) 4513.
7. C. Hou, Z. Tai, L. Zhao, Y. Zhai, Y. Hou, Y. Fan, F. Dang, J. Wang and H. Liu, *J. Mater. Chem. A*, 6 (2018) 9723.
8. Y. Zou, W. Zhang, N. Chen, S. Chen, W. Xu, R. Cai, C. L. Brown, D. Yang, X. Yao. *ACS Nano*, 13 (2019) 2062.
9. X. Fan, S. Li, L. Lu, *Electrochim. Acta,* 200 (2016) 152.
10. A. Smaldone, S. Brutti, A.D. Bonis, N. Ciarfaglia, A. Santagata, R. Teghil, *App. Surf. Sci.* , 445 (2018) 56.
11. X. Zhou, F. Cheng, J. Yang, M. Jia, A. Sun, J. Tang, *Mater. Lett.,* 234 (2019) 335.
12. Y. Wei, Z. Zi, B. Chen, B. Zhao, X. Zhu, C. Liang, X. Ma, J. Dai, *J. Alloy. Compd.* , 756 (2018) 93.
13. T. Wang, H. Li, S. Shi, T. Liu, G. Yang, Y. Chao, F. Yin, *Small*, 1 (2017) 1604182.
14. C. Liu, C. Zhang, H. Song, C. Zhang, Y. Liu, X. Nan, G. Cao, *Nano Energy*, 22 (2016) 290.
15. Y. Zou, S. Chen, X.Yang, N. Ma, Y. Xia, D. Yang, S. Guo, *Adv. Energy Mater.*, 6 (2016) 1601549.